Journal of Sound and Vibration (2002) **258**(5), 847–866
doi:10.1006/jsvi.2002.5185, available online at http://www.idealibrary.com on IDEAL®

FREE VIBRATION ANALYSIS OF BAFFLED LIQUID-STORAGE TANKS BY THE STRUCTURAL-ACOUSTIC FINITE ELEMENT FORMULATION

J. R. Cho, H. W. Lee and K. W. Kim

School of Mechanical Engineering, Pusan National University, Kumjung-Ku, Jangjeon-Dong, Pusan 609-735, *South Korea. E-mail: jrcho@hyowon.pusan.ac.kr*

(*Received* 26 *July* 2001, *and in final form* 15 *March* 2002)

In fluid–structure interaction systems, baffles as a dynamic damping device are being widely used to suppress the fluid sloshing motion. Meanwhile, natural and dynamic behaviors of such systems are significantly influenced by the baffle parameters, such as the baffle number, the installation location, the inner-hole diameter and the liquid fill height. This paper intends to numerically investigate the parametric eigen characteristics, by the coupled structural-acoustic finite element method (FEM), of baffled cylindrical liquid-storage tank. According to the symmetric two-field formulation, a test FEM program is developed, in which the reduced integration for avoiding the shear and membrane locking and the modified shear correction factor as well as degenerated 8- and 6-node shell elements and 3-D trilinear acoustic elements are used. Through the comparison with the available analytic solutions of no-baffled axisymmetric tank, the validity of the test program and theoretical work is verified. Next, with the verified test FEM program, various combinations of major baffle parameters are intensively examined, in order for the parametric baffle effects on the natural frequency of baffled tanks.

1. INTRODUCTION

For several decades, fluid–structure interaction problem has been a continuous challenging research subject in various scientific and engineering applications, such as stationary liquid storage tanks, dam–reservoir systems, nuclear reactors in fluid, fuel-storage tanks of moving vehicles, vessels in service, tower-like structures, and so on [1–3]. In the studies of fluid–structure interaction systems, major concerns are the analysis of natural and dynamic-response behaviors and the fluid motion suppression for securing the system stability. Here, we can classify the numerical approaches for the free-vibration and dynamic-response analysis into two, the coupled formulation [4, 5] and the separate formulation [6, 7] using the mass-adding technique. Even though the latter is relatively easier to implement, it is restricted to simple geometry and unsuitable for the problems with excessive flow motion.

On the other hand, various kinds of devices for suppressing the dynamic motion have been introduced, as is well classified by Welt and Modi [8]. For general engineering liquid-storage tanks, a disc-type baffle with inner hole is being widely used, because it is more practical and easy to install. However, the natural and dynamic-response behavior is significantly affected by the baffle parameters, such as the baffle number, the installation location and the inner-hole diameter [9]. So, the determination of a suitable combination of such baffle parameters becomes a crucial part in the design of a baffled liquid-storage

0022-460X/02/$35.00

tank. Meanwhile, the introduction of baffle makes the numerical analysis more complicated that the application of classical separate approach becomes too hard. From this point of view, the parametric analysis of baffled tanks by the coupled method deserves the importance.

According to our brief review of the numerical studies, Zienkiewicz and Bettess [10] introduced a coupled formulation in terms of the hydrodynamic pressure, while Everstine [11] in terms of the velocity potential. However, these formulations lead inherently to non-symmetric or complex matrix equations. In order to overcome such numerical difficulties, Morand and Ohayon [12] and Sandberg and Goransson [13] introduced the symmetric coupled formulations by mixing the hydrodynamic pressure and displacement potentials. As well, Olson and Bathe [14] derived a coupled symmetric formulation based on the fluid velocity potential. While, differing from the above investigators, Chen and Taylor [15] used displacement finite elements for both the structure deformation and the flow velocity fields in order to construct easily a coupled formulation.

However, one can realize, from the literature survey, that numerical studies performed so far have been focused mostly on no-baffled liquid-storage tanks, except for recent few works [16]. As a result, the free-vibration and dynamic-response analysis of baffled tanks has relied largely on experiments [9, 17, 18] and analytical methods with simplifications [8, 19]. Meanwhile, with current commercial finite element method (FEM) codes the coupled free-vibration analysis of baffled cases is rather restricted, in spite of the remarkable advances in numerical analysis techniques for fluid–structure interaction systems. Because, the fluid elements are limited to linear polynomial, or the hydrodynamic pressure modes are not available, or the baffle thickness dimension is not reflected. Considering these situations, development of a test program is desirable for the free-vibration study of baffled tanks.

In a series of our recent works [6, 20, 21], this paper intends to the parametric investigation on free-vibration characteristics as well as the development of a structural-acoustic finite element program for baffled cylindrical liquid-storage tanks. For the coupled symmetric structural-acoustic formulation, we approximate the free-vibration problem, with degenerated 8- and 6-node shell elements and 3-D acoustic elements, according to the symmetric two-field formulation. Furthermore, the reduced integration technique is employed for preventing the shear and membrane locking. The theoretical works and the test program are verified by comparing with the available analytical solution. And the parametric variations of the natural frequency are intensively examined through various combinations of the number and location of baffle and the inner-hole diameter as well as the liquid height.

2. BAFFLED CYLINDRICAL LIQUID-STORAGE TANK

Figure 1 illustrates a closed-type liquid-storage tank of uniform thickness t and diameter D, where liquid is filled up to the height H_L and a baffle of uniform thickness t_B and inner-hole diameter D_B is installed at the location H_B. Both of the tank and the baffle are manufactured with the same material. Throughout this paper we use two scripts L and B to stand for the liquid and the baffle, respectively, in defining material and geometry parameters.

Even though various kinds of supporting conditions for closed-type tanks are possible [2], we in this paper restrict the problem such that two circumferential edges of top and bottom plates are fixed. So, these two edges become the essential boundary part $\partial\Omega_D$ of the baffled tank structure Ω, for our main numerical analysis. Viewing the baffled tank

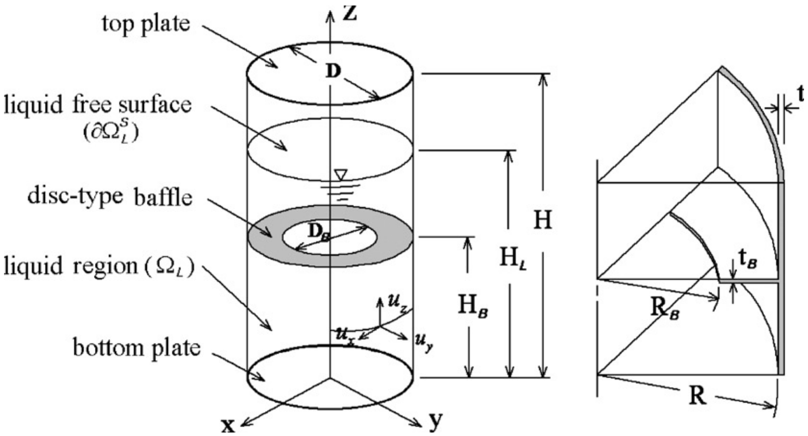

Figure 1. Geometry and symbol definition of cylindrical liquid-storage tank with a baffle.

structure as a 3-D linear elastic body, its undamped dynamic motion in Cartesian coordinates is governed by

$$\sigma_{ij}(\mathbf{u})_{,j} - \rho \frac{\partial^2 u_i}{\partial t^2} = 0 \quad \text{in } \Omega \tag{1}$$

with the boundary conditions

$$u_i = 0 \quad \text{on } \partial\Omega_D, \tag{2}$$

$$\sigma_{ij} n_j = -p n_i \quad \text{on } \partial\Omega_I. \tag{3}$$

In which, **n** indicates the outward unit vector normal to the structure boundary and $\partial\Omega_I$ the common liquid–structure interface, and p the hydrodynamic pressure. Compared to the usual no-baffled storage tanks, the liquid–structure interface of baffled cases becomes considerably complicated.

In a closed-type tank, the mean flow velocity and the flow dissipation are absent so that $\nabla \cdot \mathbf{v} = 0$; furthermore, the acoustic amplitude caused by the pressure fluctuation (i.e., acoustic pressure p_c) is relatively smaller than the mean hydrodynamic pressure p_0 [22]. Then, combining the continuity equation and the Navier–Stokes equations for irrotational inviscid compressible flows results in the well-known Helmholtz-type wave propagation equation

$$\nabla^2 p - \frac{1}{c^2}\frac{\partial^2 p}{\partial t^2} = 0 \quad \text{in } \Omega_L, \tag{4}$$

where $p = p_0 + p_c$. As for corresponding boundary conditions, we here specify as follows:

$$\nabla p \cdot \mathbf{n} = -\rho_0^L \mathbf{n} \cdot \frac{\partial^2 \mathbf{u}}{\partial t^2} \quad \text{on } \partial\Omega_I, \quad p = 0 \quad \text{on } \partial\Omega_L^S. \tag{5,6}$$

In the above equations, c is the speed of sound in fluid calculated by $\sqrt{k/\rho_0^L}$ with defining k the bulk modulus and ρ_0^L the mean density of liquid respectively.

Remark 1. According to the boundary condition specification of the wave propagation equation, the flow model is characterized. First, if we assume the structure to be rigid (i.e., letting the right-hand side (RHS) of equation (5) be zero) the flow model ends up with the classical rigid-tank sloshing model by Housner [23], then the free vibration of flow sloshing can be separately solved.

Second, the boundary specification on the liquid free surface (6) is resulted by neglecting the gravitational force. When the free-surface fluctuation by the gravitational force is taken into consideration, the modal analysis becomes frequency-dependent non-linear problem [4, 6], so that the free-vibration analysis requires a suitable numerical iteration scheme. In our previous works [6, 20], these effects, the structure flexibility and the liquid free-surface fluctuation, on the natural frequency and dynamic response are intensively assessed, by the separate numerical approach with no-baffled storage tank.

3. THIN SHELL-LIKE STRUCTURES

3.1. DEGENERATED SHELL ELEMENTS

As a 3-D continuum body, shell-like structures are characterized by the small thickness dimension compared to the other two of in-plane domain. As a result, displacement or stress field exhibits small variations through the thickness, except for the narrow regions such as boundaries of structures and junctions of members. This particular geometric feature introduces more tractable dimensionally reduced models, by restricting the order of the displacement through the thickness, such as the Kirchhoff–Love, the Reissner–Mindlin and the Koiter theories. For structures with sufficiently small thickness, the appropriateness of these first order theories has been justified. For the modelling error characteristics of usual low order models, the reader may refer to reference [24].

In the finite element analysis, these dimensionally reduced theories require a considerably small amount of degrees of freedom, when compared to the fully 3-D elasticity theory. Needless to say, it is because the displacement field in the thickness direction is assumed *a priori*. But, these theories were originated for the analytic analysis, so the numerical implementation of such theories becomes quite complicated, particularly when structures are composed of several substructures or arbitrary shaped. In order to overcome this complexity, while providing the advantage in the total degrees of freedom, Ahmad *et al.* [25] proposed the degenerated shell element.

Differing from the above-mentioned low order theories, the degenerated 8- and 6-node shell elements were derived respectively from general 20- and 15-node 3-D finite elements in Cartesian co-ordinates, so that those can be easily implemented for general shell-like structures [26]. As is well described in reference [25], four coordinate systems are used for this element: global co-ordinates $\{x, y, z\}$, curvilinear co-ordinates $\{\xi, \eta, \zeta\}$, nodal co-ordinates $\{\theta_1, \theta_2, \theta_3\}$, and the local co-ordinates $\{x', y', z'\}$ for defining local strains and stresses. Here, curvilinear co-ordinates maps into a master element defined within a cubic of $[-1,\ 1]^3$ while nodal co-ordinates indicates three unit vectors tangent to curvilinear co-ordinates. On the other hand, for each node three in-plane translation components $\{\bar{u}, \bar{v}, \bar{w}\}$ in global co-ordinates and two rotation components of the mid-plane $\{\bar{\alpha}_1, \bar{\alpha}_2\}$ in nodal co-ordinates are assigned.

We basically adopt the degenerated 8- and 6-node shell elements for our test FEM program, and we describe the ingredients associated with our study. The geometry of a shell element in global co-ordinates, is approximated using iso-parametric finite element basis functions such that

$$x_i = \sum_{k=1}^{6,8} \varphi_k(\xi, \eta)\left\{\bar{x}_i^k + \frac{t}{2}\zeta\theta_{3i}^k\right\}, \quad i = x, y, z, \tag{7}$$

where $\{\bar{x}^k, \bar{y}^k, \bar{z}^k\}$ are the nodal in-plane co-ordinates, and $\{\theta_{3x}^k, \theta_{3y}^k, \theta_{3z}^k\}$ the nodal value of global components of the unit normal vector θ_3 of node k. Similarly, the displacement field

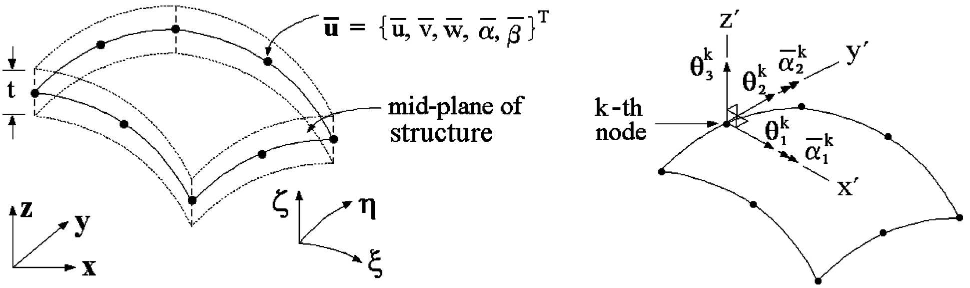

Figure 2. Degenerated 8-node shell element: (a) global and curvilinear co-ordinates; (b) nodal and local co-ordinates.

is approximated using the same iso-parametric basis functions and the nodal values consisting of three in-plane and two rotational degrees of freedom

$$u_i = \sum_{k=1}^{6,8} \varphi_k(\xi,\eta)\left\{\bar{u}_i^k + [-\theta_{2i}^k\bar{\alpha}_1^k + \theta_{1i}^k\bar{\alpha}_2^k]\frac{t}{2}\zeta\right\}, \quad i = x, y, z. \tag{8}$$

Local strains and stresses are defined first in local co-ordinates $\{x', y', z'\}$, another Cartesian co-ordinates for which nodal co-ordinates become unit vectors. Then, local quantities (displacement, strains and stresses) are transformed by the co-ordinate transformation tensor β_{ij}, and which is also interpolated using iso-parametric basis functions

$$\beta_{ij} = \frac{\partial x_i}{\partial x'_j}, \quad \beta_{ij} = \sum_{k=1}^{6,8} \bar{\beta}_{ij}^k \varphi_k(\xi,\eta). \tag{9}$$

Within the local co-ordinates, strains and stresses are defined as follows:

$$\varepsilon'_{ij} = (u'_{i,j} + u'_{j,i})/2, \quad \boldsymbol{\sigma}' = \mathbf{E}'\boldsymbol{\varepsilon}', \quad \mathbf{E}' = \frac{E}{(1-\nu^2)}\begin{bmatrix} \mathbf{E}'_1 & 0 \\ 0 & \mathbf{E}'_2 \end{bmatrix}, \tag{10, 11}$$

where $\boldsymbol{\varepsilon}'$ and $\boldsymbol{\sigma}'$ are (6×1) vectors of Cauchy strain and stress tensors, respectively, and furthermore

$$\mathbf{E}'_1 = \begin{bmatrix} 1 & \nu & 0 \\ \nu & 1 & 0 \\ 0 & 0 & 0 \end{bmatrix}, \quad \mathbf{E}'_2 = \frac{1-\nu}{2}\begin{bmatrix} 1 & 0 & 0 \\ 0 & 1/\kappa & 0 \\ 0 & 0 & 1/\kappa \end{bmatrix}. \tag{12}$$

The modified shear correction factor (MSCF) is determined by $\kappa = \max[1.2, (1 + A_{mid}/125t^2)]$.

Since we approximate the displacement in the global co-ordinates, local strains and stresses are transformed to those defined in the global co-ordinates according to

$$\boldsymbol{\varepsilon}' = \mathbf{T}\boldsymbol{\varepsilon}, \quad \boldsymbol{\sigma}' = \mathbf{T}\boldsymbol{\sigma} \tag{13}$$

in which $\mathbf{T}$ is the (6×6) transformation matrix [27]. As well as, the total strain energy is defined by global quantities with a help of the transformed material coefficient matrix such that

$$U = \frac{1}{2}\int_\Omega \boldsymbol{\varepsilon}'^{\mathrm{T}}\boldsymbol{\sigma}'\,\mathrm{d}V = \frac{1}{2}\int_\Omega \boldsymbol{\varepsilon}^{\mathrm{T}}\mathbf{E}\boldsymbol{\varepsilon}\,\mathrm{d}V, \quad \mathbf{E} = \mathbf{T}^{\mathrm{T}}\mathbf{E}'\mathbf{T}. \tag{14}$$

3.2. NUMERICAL LOCKING AND REDUCED INTEGRATION

In the numerical analysis of thin elastic structures, such as beam-, arch-, plate- and shell-like structures, using standard finite element scheme, the approximation quality may deteriorate significantly when the finite element approximation space is poor (low approximation orders or/and coarse meshes). In computational mechanics, this numerical locking has been treated as an important research subject, so that its remedies as well as the mathematical clearing up of its cause have been presented through numerous publications. In general, the problems with inherent constraints may experience the numerical locking phenomenon, as the characteristic problem parameter approaches its limit with poor approximation spaces [28].

In structural analysis, the problem parameter becomes the thickness dimension, while shear constraints for structures of vanishing curvatures: $\varepsilon'_{31} = \varepsilon'_{32} = 0$, and shear and membrane constraints for structures of non-vanishing curvatures: $\varepsilon'_{31} = \varepsilon'_{32} = 0$ and $\varepsilon'_{11} = \varepsilon'_{12} = \varepsilon'_{22} = 0$. In order words, these constraints are satisfied while making the approximate displacement field be almost null space as the structure thickness approaches zero, when the approximation space is not sufficiently rich [29]. As a result, the static analysis produces significantly small displacements while the free vibration too much high natural frequencies.

Remark 2. Shear and membrane locking possess the following characteristics. First, the numerical locking prevails only for the bending-dominated structures (BDS) so that the membrane-dominated structures (MDS) are locking-free. Second, the numerical locking is independent of analysis models, so that it is related to not the approximation order in the thickness direction, but the in-plane approximation order. Third, shell-like structures experience more severe numerical locking than plate-like structures owing to additional membrane locking. For the detailed discussion, the reader may refer to [29].

Among several useful techniques for overcoming shear-membrane locking in shell-like structures, we adopt the reduced integration (RI) technique originated by Zienkiewicz *et al.* [30]. Since it does not require other special treatments in the finite element formulation that it has been known to be suitable for general thin elastic structures. Figure 3 depicts reduced Gauss points for degenerated 8- and 6-node shell elements used in this study. On the other hand, we use exact Gauss points for the numerical integration through the thickness.

4. STRUCTURAL-ACOUSTIC FREE-VIBRATION APPROXIMATIONS

4.1. COUPLED SYMMETRIC FORMULATION

For finite element approximations of undamped dynamic equation (1) and wave equation (4), we express the dynamic displacement $\mathbf{u}$ and the hydrodynamic pressure p such that

$$\mathbf{u} = \Phi\bar{\mathbf{u}}, \quad p = \Psi\bar{\mathbf{p}}. \tag{15}$$

Referring to equation (8), together with Figure 2, Φ becomes a $(3 \times 5N_S)$ matrix containing 2-D iso-parametric basis functions $\varphi_k(\xi, \eta)$ of number N_S such that

$$\Phi = \left[\begin{pmatrix} \\ \cdots\cdots \\ \\ \end{pmatrix} \cdots \begin{pmatrix} \varphi_k & 0 & 0 & -\theta^k_{21} t\zeta\varphi_k/2 & \theta^k_{11} t\zeta\varphi_k/2 \\ 0 & \varphi_k & 0 & -\theta^k_{22} t\zeta\varphi_k/2 & \theta^k_{12} t\zeta\varphi_k/2 \\ 0 & 0 & \varphi_k & -\theta^k_{23} t\zeta\varphi_k/2 & \theta^k_{13} t\zeta\varphi_k/2 \end{pmatrix} \cdots \begin{pmatrix} \\ \cdots\cdots \\ \\ \end{pmatrix} \right]. \tag{16}$$

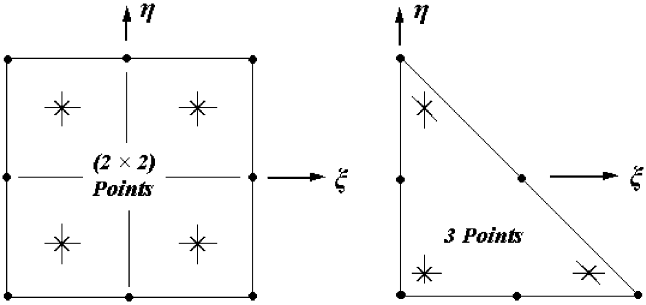

Figure 3. Gauss integration points reduced for degenerated 8- and 6-node shell elements.

Furthermore, Ψ is a $(1 \times N_L)$ matrix composed of 3-D iso-parametric basis functions $\psi_k(\xi, \eta, \zeta)$ of number N_L for the hydrodynamic pressure.

Then the finite element approximation of undamped structural dynamic motion subjected by the internal hydrodynamic pressure leads to

$$\mathbf{K}_S \bar{\mathbf{u}} + \mathbf{M}_S \ddot{\bar{\mathbf{u}}} - \mathbf{Q}\bar{\mathbf{p}} = \mathbf{0} \tag{17}$$

with matrices defined by

$$\mathbf{K}_S = \int_{\Omega} (\mathbf{D}\Phi)^{\mathrm{T}} \mathbf{E} (\mathbf{D}\Phi) \, \mathrm{d}V, \quad \mathbf{M}_S = \rho \int_{\Omega} \Phi^{\mathrm{T}} \Phi \, \mathrm{d}V, \quad \mathbf{Q} = \int_{\partial\Omega_I} \Phi^{\mathrm{T}} \mathbf{N} \Psi \, \mathrm{d}s. \tag{18, 19, 20}$$

In which, $\mathbf{D}$ refers to the divergence-like differential operator defining Cauchy strains, and $\mathbf{N} = \{n_x, n_y, n_z\}^{\mathrm{T}}$ at the structure boundary. On the other hand, the finite element approximation of hydrodynamic pressure field of liquid contained within the flexible tank ends up with

$$\mathbf{K}_L \bar{\mathbf{p}} + \mathbf{M}_L \ddot{\bar{\mathbf{p}}} + \rho_0^L \mathbf{Q}^{\mathrm{T}} \ddot{\bar{\mathbf{u}}} = \mathbf{0} \tag{21}$$

with

$$\mathbf{K}_L = \int_{\Omega_L} (\nabla\Psi)^{\mathrm{T}} (\nabla\Psi) \, \mathrm{d}V, \quad \mathbf{M}_L = \frac{1}{c^2} \int_{\Omega_L} \Psi^{\mathrm{T}} \Psi \, \mathrm{d}V. \tag{22, 23}$$

Combining two-matrix equations (17) and (21), together with harmonic motion assumptions, we arrive at the coupled free-vibration matrix system for structural-acoustic problems.

$$\begin{bmatrix} \mathbf{K}_S & -\mathbf{Q} \\ \mathbf{0} & \mathbf{K}_L \end{bmatrix} \begin{Bmatrix} \bar{\mathbf{u}} \\ \bar{\mathbf{p}} \end{Bmatrix} - \omega^2 \begin{bmatrix} \mathbf{M}_S & 0 \\ \rho_0^L \mathbf{Q} & \mathbf{M}_L \end{bmatrix} \begin{Bmatrix} \bar{\mathbf{u}} \\ \bar{\mathbf{p}} \end{Bmatrix} = \begin{Bmatrix} \mathbf{0} \\ \mathbf{0} \end{Bmatrix}. \tag{24}$$

Owing to the non-symmetry, this matrix system requires expensive computation from a point of matrix-array storage space and computation time. Hence, we symmetrize it according to the simple three-field formulation technique proposed by Morand and Ohayon [12], for which a fluid displacement potential q is additionally introduced such that $q : p = -\rho_0^L \ddot{q}$. Then, we have additional matrix equations given by

$$\mathbf{M}_L \bar{\mathbf{p}} - \omega^2 \rho_0^L \mathbf{M}_L \bar{\mathbf{q}} = \mathbf{0}. \tag{25}$$

According to the introduction of the fluid displacement potential, the above non-symmetric matrix equation (24) is changed to a coupled symmetric one in terms of three fields:

$$\begin{bmatrix} \mathbf{K}_S & \mathbf{0} & \mathbf{0} \\ \mathbf{0} & \mathbf{M}_L/\rho_0^L & \mathbf{0} \\ \mathbf{0} & \mathbf{0} & \mathbf{0} \end{bmatrix} \begin{Bmatrix} \bar{\mathbf{u}} \\ \bar{\mathbf{p}} \\ \bar{\mathbf{q}} \end{Bmatrix} - \omega^2 \begin{bmatrix} \mathbf{M}_S & \mathbf{0} & \rho_0^L \mathbf{Q} \\ \mathbf{0} & \mathbf{0} & \mathbf{M}_L \\ \rho_0^L \mathbf{Q}^{\mathrm{T}} & \mathbf{M}_L & -\rho_0^L \mathbf{K}_L \end{bmatrix} \begin{Bmatrix} \bar{\mathbf{u}} \\ \bar{\mathbf{p}} \\ \bar{\mathbf{q}} \end{Bmatrix} = \begin{Bmatrix} \mathbf{0} \\ \mathbf{0} \\ \mathbf{0} \end{Bmatrix}. \tag{26}$$

The stiffness matrix $\mathbf{K}_L$ of liquid is guaranteed to be positive definite by the essential boundary condition (6) specified on the liquid free surface. Hence, we can apply the static condensation to eliminate the fluid displacement potential from equation (26). Then, we have

$$\bar{\mathbf{q}} = \mathbf{K}_L^{-1}(\mathbf{M}_L \bar{\mathbf{p}}/\rho_0^L + \mathbf{Q}^{\mathrm{T}} \bar{\mathbf{u}}) \tag{27}$$

and, the coupled symmetric two-field form reduced further, for the structural-acoustic free-vibration analysis, given by

$$\begin{bmatrix} \mathbf{K}_S & \mathbf{0} \\ \mathbf{0} & \mathbf{M}_L/\rho_0^L \end{bmatrix} \begin{Bmatrix} \bar{\mathbf{u}} \\ \bar{\mathbf{p}} \end{Bmatrix} - \omega^2 \begin{bmatrix} \mathbf{M}_S + \rho_0^L \mathbf{Q}\mathbf{K}_L^{-1}\mathbf{Q}^{\mathrm{T}} & \mathbf{Q}\mathbf{K}_L^{-1}\mathbf{M}_L \\ (\mathbf{Q}\mathbf{K}_L^{-1}\mathbf{M}_L)^{\mathrm{T}} & \mathbf{M}_L\mathbf{K}_L^{-1}\mathbf{M}_L/\rho_0^L \end{bmatrix} \begin{Bmatrix} \bar{\mathbf{u}} \\ \bar{\mathbf{p}} \end{Bmatrix} = \begin{Bmatrix} \mathbf{0} \\ \mathbf{0} \end{Bmatrix}. \tag{28}$$

In which the symmetry of two matrices, $\mathbf{K}_L$ and $\mathbf{M}_L$, is used.

Remark 3. First, for incompressible liquid motion without considering the free-surface fluctuation, $\mathbf{M}_L$ becomes identically a zero matrix according to $1/c^2 = 0$. As a result, the coupled free-vibration matrix system reduces to the separate one for hydroelastic free-vibration problems:

$$\mathbf{K}_S \bar{\mathbf{u}} - \omega^2 \{\mathbf{M}_S + \rho_0^L \mathbf{Q}\mathbf{K}_L^{-1}\mathbf{Q}^{\mathrm{T}}\} \bar{\mathbf{u}} = \mathbf{0}. \tag{29}$$

Furthermore, the mass term $(\rho_0^L \mathbf{Q}\mathbf{K}_L^{-1}\mathbf{Q}^{\mathrm{T}})$ is nothing but the corresponding added mass matrix, as presented in our previous works [6, 20]. Second, one can realize, from equations (28) and (29), that the hydrodynamic interaction, for structural-acoustic problems without considering the free-surface fluctuation, is caused by the mean hydrodynamic pressure p_0 (i.e., added mass in equation (29)) and the acoustic wave pressure p_c (three mass terms in equation (28) multiplied by $\mathbf{M}_L$). Third, differing from the incompressible case, the structural-acoustic free vibration cannot be analyzed separately.

4.2. DEVELOPMENT OF TEST FEM PROGRAM

According to the theoretical results described so far, we developed a test finite element program based on Pentium PC, in which mass matrix is not lumped so that upper triangular part of full mass matrix is stored. Meanwhile, we employ the Lanczos transformation to reduce the original eigen matrix system for a truncated one, which is three times as large as the number of desired natural frequencies. The final truncated eigenmatrix system is solved by the Jacobi iteration method.

In addition, we developed our own pre-processor for generating finite element meshes using degenerated 8- and 6-node shell elements for the structure and 20- and 15-node solid elements for the liquid domain. Figure 4 illustrates structure and liquid meshes generated for a closed tank with three baffles. We note here that structure and liquid meshes have the same mesh partition over the common liquid–structure interface $\partial\Omega_I$, so that the nodal value interaction is easily implemented without other interpolation techniques. On the other hand, mode shapes are visualized with MSC/PATRAN by introducing a user-defined interface module written in Patran Command Language (PCL).

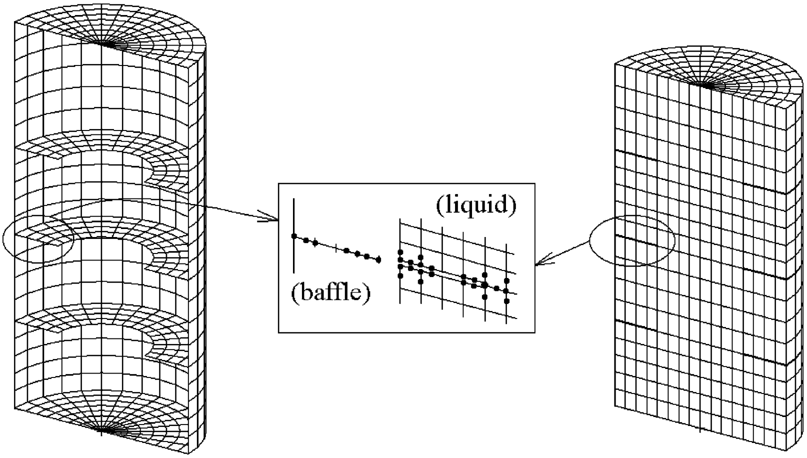

Figure 4. Finite element meshes for closed tank with three baffles and interior liquid.

5. NUMERICAL EXPERIMENTS

In order to verify the reliability and robustness of the test program developed for our parametric investigation, we first compare the numerical results with the analytical solutions for a no-baffled axisymmetric cylindrical liquid-storage tank, for various tank heights, liquid fill heights and the structure thicknesses. After the program verification, we perform the parametric numerical experiments for closed-type baffled tanks shown in Figure 1, for various combinations of baffle parameters, the baffle number, the baffle location and the baffle inner-hole diameter, as well as the liquid fill height.

5.1. VERIFICATION EXPERIMENTS

Referring to Figure 5(a), the first model tank for the program verification is open at the top and clamped at the bottom, and furthermore it does not have a baffle. On the other hand, we consider three tank heights H/R : 0·5, 1·0 and 2·0, and four liquid fill heights H_L/H : 0·25, 0·5, 0·75 and 1·0, so that total of 12 combinations are examined. From the problem symmetry, we consider a quarter for the axisymmetric free-vibration analysis, for which the structure mesh is composed of 120 uniform degenerated 8-node shell elements (10 in the circumferential direction while 12 in the axial direction). While the liquid meshes are uniformly partitioned with 15- and 20-node solid elements, according to the liquid fill height, such that 120 $(4 \times 10 \times 3)$, 240 $(4 \times 10 \times 6)$, 360 $(4 \times 10 \times 9)$ and 480 $(4 \times 10 \times 12)$, respectively (in the radial direction × in the circumferential direction × in the axial direction). However, structure and liquid mesh partition numbers do not vary along the relative tank height. Material and geometry data taken for verification experiments are summarized in Table 1, where the structure thickness and the liquid fill height are taken variable.

In Table 2, we record three lowest axisymmetric natural frequencies of the first model problem for 12 simulation combinations. The analytic values are computed according to our previous work [21], which has been derived, for the free-vibration analysis of no-baffled axisymmetric cylindrical liquid-storage tanks, by combining the Novozhilov shell theory and the inviscid compressible flow. Therefore, it covers empty, partially filled and completely filled liquid-storage tanks as well as the incompressible case. Errors in Table 2

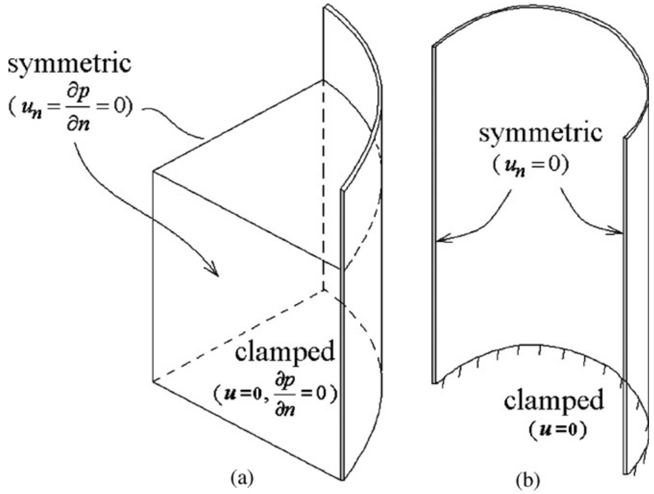

Figure 5. Model problems for verification experiments: (a) a quarter of no-baffled open-type axisymmetric liquid-storage tank (for the accuracy verification); (b) a half of open-type empty cylindrical tank (for the shear-membrane locking verification).

TABLE 1

Material and geometry data taken for the verification simulation

	Material data		Geometry data	(m)
Structure	Density $(\rho)(\mathrm{kg/m^3})$	7·85 (E+03)	Radius of tank (R)	20
	Young's modulus (E) (Pa)	2·15 (E+11)	Height of tank (H)	10, 20, 40
	Poisson ratio (v)	0·3	Thickness (t, t_B)	0·0283
Liquid	Mean density (ρ_0^L) $(\mathrm{kg/m^3})$	1·0 (E+03)	(also, variable)	
	Bulk modulus (k) (Pa)	1·99 (E+09)	Liquid height (H_L)	Variable

refer to the relative error defined by

$$\eta = \frac{\omega^{FEM} - \omega^{Analytic}}{\omega^{Analytic}} \times 100(\%). \tag{30}$$

From the comparative numerical results, analytic and numerical results show a good agreement with the maximum relative error less than 3%. Therefore our theoretical works and the test program are proved to analyze the structural-acoustic free vibration with the reliable accuracy, for a wide range of liquid fill and tank heights. Figures 6 and 7 presents mode shapes of the structure and the hydrodynamic pressure, respectively, for three lowest natural frequencies of the axisymmetric liquid-storage tank with $H/R = 2{\cdot}0$ and $H_L/H = 1{\cdot}0$.

Next, we examine the robustness of the test FEM program against the shear-membrane locking. We note here that the previous axisymmetric vibration is membrane-dominated so that we did not experience any noticeable numerical locking in axisymmetric natural frequencies to the shell thickness decrease. As mentioned earlier, the shear-membrane locking occurs only for the bending-dominated cases, and furthermore it is independent of

TABLE 2

Comparison between axisymmetric natural frequencies (rad/s) by analytic [21] *and test FEM program*

Liquid fill height (H_L/H)		Slenderness of liquid-storage tank (H/R)								
		2·0			1·0			0·5		
		First	Second	Third	First	Second	Third	First	Second	Third
0·25	Analytic	45·46	82·04	104·56	70·71	122·56	163·27	112·56	212·71	261·58
	FEM	45·45	82·54	107·50	70·85	126·03	165·11	115·64	214·80	261·90
	Error(%)	−0·02	0·60	2·81	0·20	2·83	1·13	2·66	0·98	0·12
0·5	Analytic	27·03	56·08	73·26	46·03	82·05	105·56	70·71	120·56	163·27
	FEM	27·31	56·02	73·61	45·48	82·56	108·15	70·88	122·91	164·30
	Error(%)	1·03	−0·11	0·48	−1·19	0·62	2·45	0·23	1·95	0·63
0·75	Analytic	18·94	43·90	58·93	34·02	65·95	85·02	54·87	95·77	122·45
	FEM	19·28	44·52	58·89	34·22	65·94	85·69	54·88	97·25	122·71
	Error(%)	1·81	1·42	−0·18	0·61	−0·01	0·79	0·01	1·55	0·21
1·0	Analytic	14·48	36·17	49·97	27·03	56·08	73·26	45·46	82·01	104·41
	FEM	14·79	36·33	49·95	27·35	56·04	74·63	45·53	82·51	106·34
	Error(%)	2·19	0·43	−0·04	1·18	−0·06	1·87	0·15	0·60	1·85

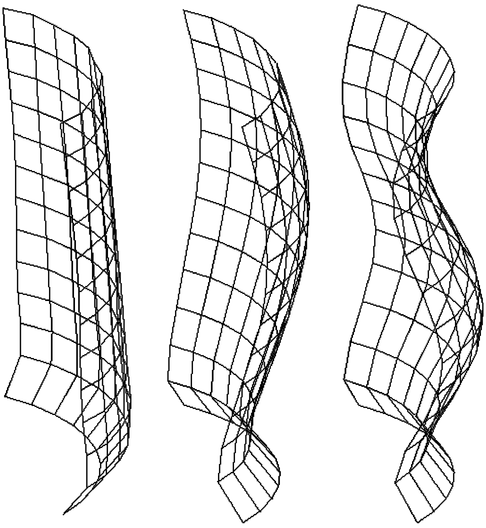
(a) (b) (c)

Figure 6. Mode shapes of the structure ($H/R = 2{\cdot}0$ and $H_L/H = 1{\cdot}0$): (a) first mode (14·7931 rad/s); (b) second mode (32·3263 rad/s); and (c) third mode (49·9474 rad/s).

whether liquid is filled or not. Hence, we select the model problem shown in Figure 5(b) that is surely a bending-dominated free-vibration problem. Regardless of the relative shell thickness t/R, finite element meshes are constructed with uniform 400 (20×20) degenerated 8-node shell elements.

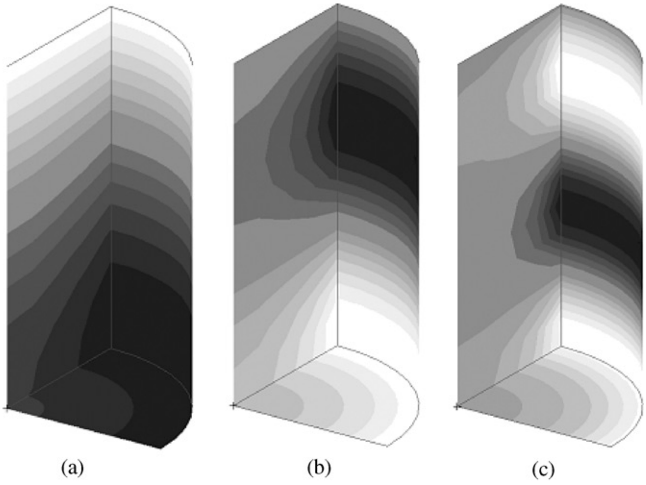

Figure 7. Mode shapes of the hydrodynamic pressure ($H/R = 2{\cdot}0$ and $H_L/H = 1{\cdot}0$): (a) first mode (14·7931 rad/s); (b) second mode (32·3263 rad/s); and (c) third mode (49·9474 rad/s).

In Figure 8, we plot relative errors to the reference frequencies in two lowest natural frequencies, according to four methods, to the relative shell thickness. Where, reference frequencies are obtained by MSC/NATRAN with uniform 10,000 (100 × 100) quadratic shell elements. The test FEM program, combined the reduced integration (RI) and the modified shear correction factor (MSCF) with degenerated shell elements, produces natural frequencies consistent well with those by MSC/NASTRAN, so that it is confirmed to be locking free. But, the natural frequencies by the other two become considerably larger than the reference frequencies, with the thickness decrease, so that those experience severe numerical locking in the bending-dominated free-vibration analysis.

5.2. PARAMETRIC EXPERIMENTS

With closed-type tanks clamped at circumferential edges of top and bottom plates, as shown in Figure 1, we perform the parametric free-vibration analysis, with respect to the liquid fill height, the baffle number, the baffle location and the baffle inner-hole diameter. Material and geometry data are given in Table 3, which are taken from usual cylindrical fuel-storage tanks of moving vehicles. Referring to Figure 1, we consider a half of tank model for the free-vibration analysis.

We first carry out the parametric experiment with respect to six liquid fill heights: $H_L/H = 0{\cdot}2$, 0·4, 0·6, 0·8 and 0·9. Referring to Figure 9, structure mesh is uniformly partitioned with 352 degenerated shell elements ($16 \times 12 + 2 \times (5 \times 16)$) while liquid meshes constructed with 20- and 15-node elements are varying with the liquid fill height as follows: 320 ($5 \times 16 \times 4$), 480 ($5 \times 16 \times 6$), 640 ($5 \times 16 \times 8$), 800 ($5 \times 16 \times 10$) and 880 ($5 \times 16 \times 11$). In Table 4, we record lowest 10 natural frequencies, where LPD indicates the bottom-plate-dominated mode, UPD the top-plate-dominated mode, SSD the side-shell-dominated mode, and MIX the mixed mode. Structural and corresponding hydrodynamic-pressure mode shapes, for lowest natural frequencies of four distinguished modes when $H_L/H = 0{\cdot}8$, are presented in Figures 9 and 10 respectively.

We first realize, from Table 4, that the natural frequency decreases uniformly in proportional to the liquid fill height increase, and the LPD mode becomes the lowest mode

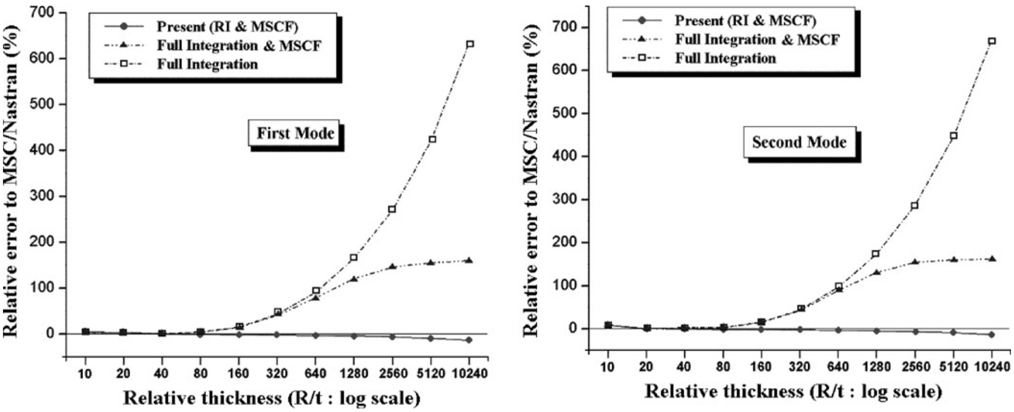

Figure 8. Variation of natural frequencies of the open-type empty cylindrical tank to the shell thickness: (a) first mode; (b) second mode.

TABLE 3

Material and geometry data taken for the parametric simulation

	Material data		Geometry data	(m)
Structure	Density (ρ)(kg/m^3)	2·78 (E + 03)	Radius of tank (R)	0·2
	Young's modulus (E) (Pa)	7·24 (E + 10)	Height of tank (H)	1·0
	Poisson ratio (ν)	0·33	Shell thickness (t)	0·00254
Liquid	Mean density (ρ_0^L)(kg/m^3)	8·149 (E + 02)	Baffle thickness (t_B)	0·003
	Bulk modulus (k) (Pa)	2·20 (E + 09)	Inner-hole radius (R_B)	Variable
	Speed of sound (c) (m/s)	1·643 (E + 03)	Liquid height (H_L)	Variable

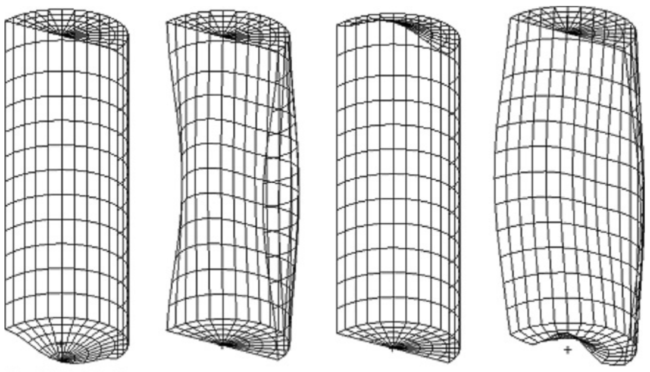

1st LPD Mode *109.0294 rad/s* (a)
1st SSD Mode *671.2814 rad/s* (b)
1st UPD Mode *774.6249 rad/s* (c)
1st MIX Mode *1109.1764 rad/s* (d)

Figure 9. Structural mode shapes of four lowest natural frequencies ($H_L/H = 0{\cdot}8$): (a) LPD mode; (b) SSD mode; (c) UPD mode; and (d) MIX mode.

Table 4

Natural frequencies (rad/s) of the no-baffled closed-type tank with respect to the liquid fill height

Mode	Relative liquid fill height (H_L/H)				
	0·2	0·4	0·6	0·8	0·9
1	195·51(L)	148·40(L)	124·29(L)	109·03(L)	103·23(L)
2	668·01(L)	658·67(L)	658·64(L)	658·83(L)	658·91(L)
3	774·62(U)	774·62(U)	756·73(S)	671·28(S)	661·50(S)
4	1074·52(L)	1023·68(S)	774·62(U)	727·85(S)	714·57(S)
5	1339·52(L)	1041·54(L)	833·18(S)	774·62(U)	774·62(U)
6	1565·44(S)	1142·78(S)	1014·20(S)	929·15(S)	918·14(S)
7	1778·37(S)	1285·93(S)	1027·46(L)	1018·39(L)	1014·69(L)
8	1938·13(U)	1320·82(L)	1274·28(M)	1109·18(M)	1081·20(S)
9	2016·52(M)	1655·53(S)	1336·55(L)	1317·71(L)	1276·30(S)
10	2072·22(M)	1814·97(M)	1459·07(S)	1333·90(S)	1295·64(S)

Note: (L): LPD mode, (U): UPD mode, (S): SSD mode, (M): MIX mode.

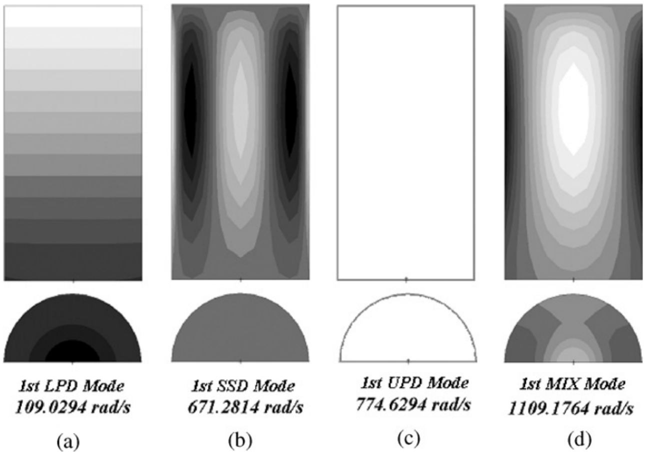

Figure 10. Corresponding hydrodynamic-pressure mode shapes of lowest natural frequencies ($H_L/H = 0{\cdot}8$): (a) LPD mode; (b) SSD mode; (c) UPD mode; and (d) MIX mode.

among four distinguished modes regardless of the liquid fill height. According to the liquid fill height increase, the SSD mode appears at lower modes, but the UPD mode shows the reverse trend. On the other hand, the MIX mode appears at higher modes as a whole. The UPD mode is independent of liquid motion, so that corresponding natural frequency remains unchanged with the liquid fill height and corresponding hydrodynamic-pressure mode does not appear, as shown in Figure 10(c). Meanwhile, referring to Figure 10, the SSD mode does not produce the spatial variation in hydrodynamic pressure at the bottom plate, differing from the LPD and MIX modes. Therefore, the model problem clearly exhibits four distinguished modes.

We also compare lowest natural frequencies of three distinguished modes, in Figure 11(a), with respect to the relative liquid fill height. According to the hydrodynamic

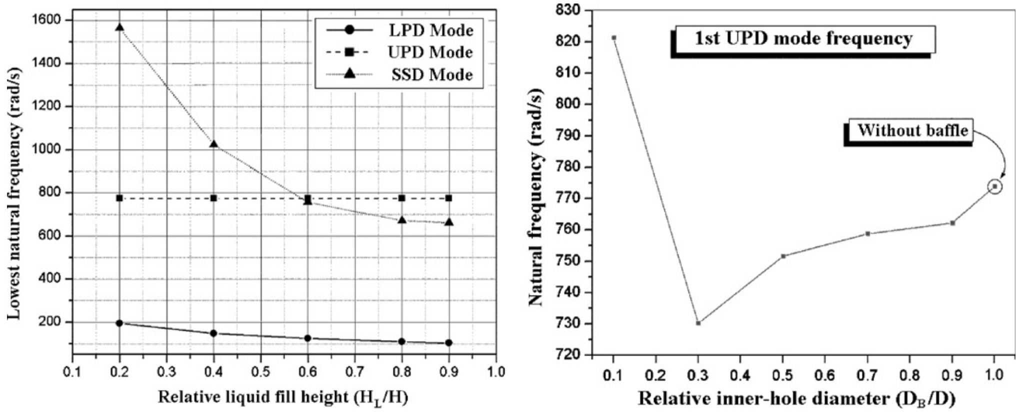

Figure 11. Variations of lowest natural frequencies: (a) three distinguished modes; (b) UPD mode to the relative inner-hole diameter (one baffle case with $H_B/H_L = 0{\cdot}5$ and $H_L/H = 0{\cdot}9$).

TABLE 5

Variation of natural frequencies to the baffle number

Baffle number	Ten lowest natural frequencies (rad/s)									
	First	Second	Third	Fourth	Fifth	Sixth	Seventh	Eighth	Ninth	10th
0	103·1	659·4	664·5	715·4	773·8($^{+}$)	929·3	1017·1	1081·7	1293·4	1302·6
1	83·0	155·3	274·6	481·5	662·3	751·6($^{+}$)	783·0	1015·1	1206·9	1303·5
2	64·5	158·3	273·6	493·2	658·3	661·0	751·6($^{+}$)	816·3	884·1	1026·8
3	56·8	144·2	263·4	477·8	557·6	658·3	669·4	751·6($^{+}$)	783·5	800·7

†UPD mode.

interaction, lowest natural frequencies of the LPD and SSD modes decrease with the relative liquid fill height, but the variation of the LPD mode is significantly smaller than the SSD mode. As a result, the SSD and MIX modes are significantly influenced by the liquid fill height.

We next examine the parametric effect of the baffle number on the natural frequency, for which we install one baffle at $H_B/H = 0{\cdot}5$, two baffles at $H_B/H = 0{\cdot}3$ and 0·6, three baffles at $H_B/H = 0{\cdot}25$, 0·5 and 0·75 respectively. But, the baffle thickness, the relative inner-hole diameter and the relative liquid fill height are fixed: $t_B = 0{\cdot}003\,\mathrm{m}$, $D_B/D = 0{\cdot}5$ and $H_L/H = 0{\cdot}9$. As well, structure and liquid meshes except for those of baffles are kept same. But, structure and liquid meshes are slightly coarser than the previous no baffle case owing to additional mesh partition requirement for baffles under given computer limitation.

Ten lowest natural frequencies, for three cases together with the no-baffle case, are represented in Table 5. As a whole, natural frequency decreases as the baffle number increases, in particularly from the no-baffle case to the one-baffle case in relatively lower frequency range. However, all three baffled cases start with the natural mode dominated by the bottom plate and the lowest baffle, so that the hydrodynamic effect on baffle becomes the most critical at the lowest baffle. Meanwhile, we experience that the lowest UPD-mode frequency is not sensitive to the baffle number and location but only to the baffle inner-hole diameter, as presented in Figure 11(b).

From Figures 12 to 14, together with Table 4, we see that the appearance order of the first UPD mode with the same natural frequency, which produces zero hydrodynamic-pressure mode, delays by one with the baffle number increase. Needless to say, it is because the baffle-dominated modes which are more flexible than the top plate appear additionally with the baffle number increase, as can be observed from Figures 12 to 14.

Finally, we examine the effects of the baffle location and the inner-hole diameter on the fundamental frequency. For this parametric investigation, we consider one baffle case with

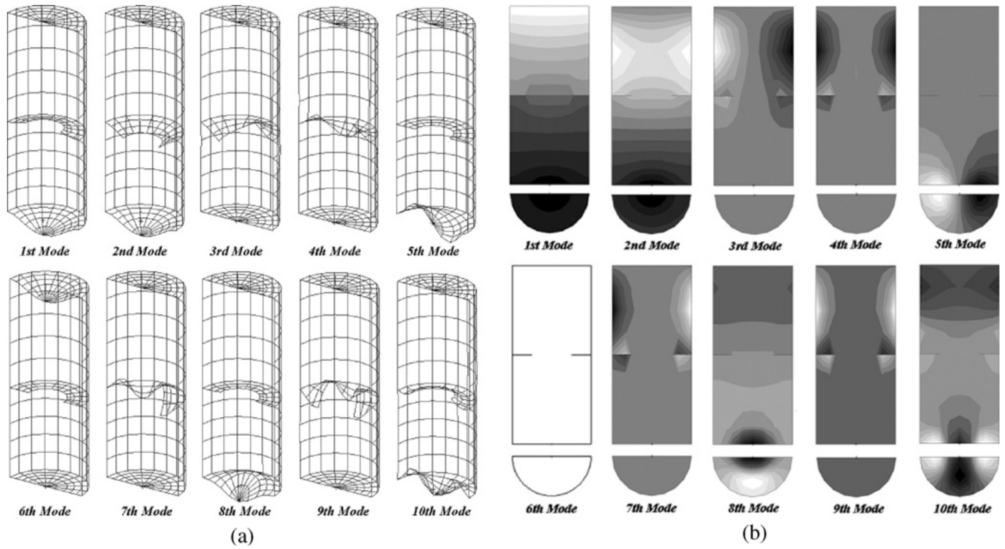

Figure 12. Mode shapes of 10 lowest natural frequencies (one baffle): (a) structure; (b) hydrodynamic pressure of liquid.

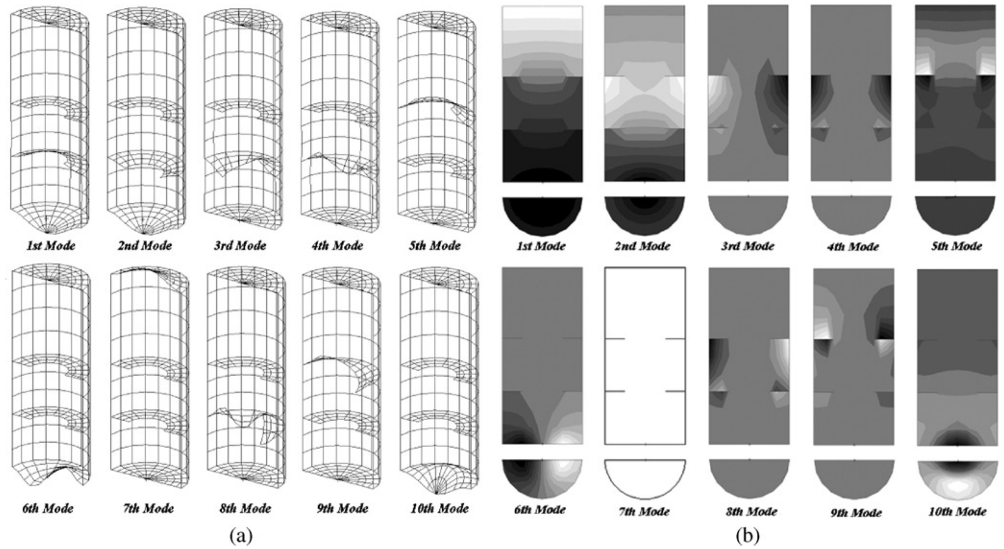

Figure 13. Mode shapes of 10 lowest natural frequencies (two baffles): (a) structure; (b) hydrodynamic pressure of liquid.

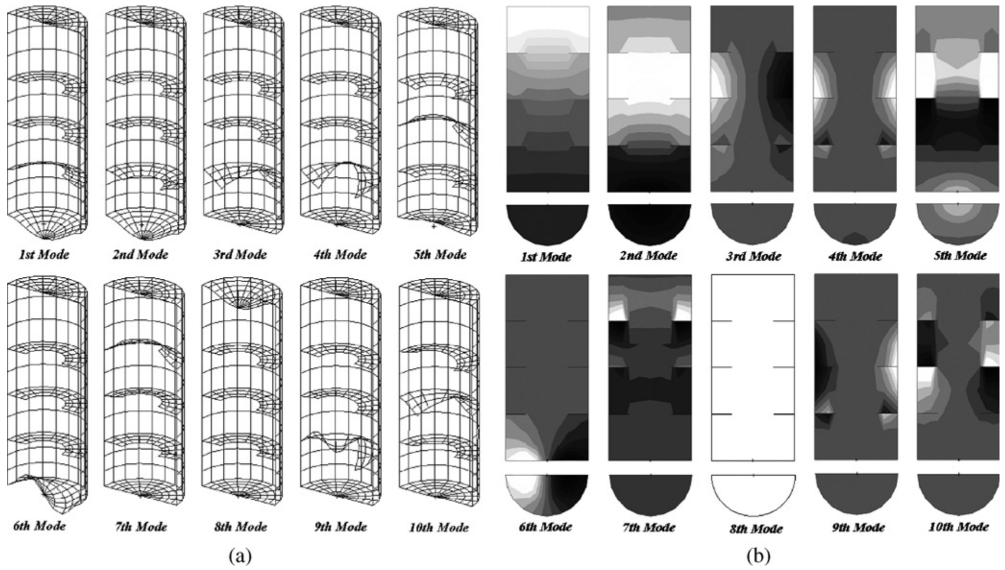

Figure 14. Mode shapes of 10 lowest natural frequencies (three baffles): (a) structure; (b) hydrodynamic pressure of liquid.

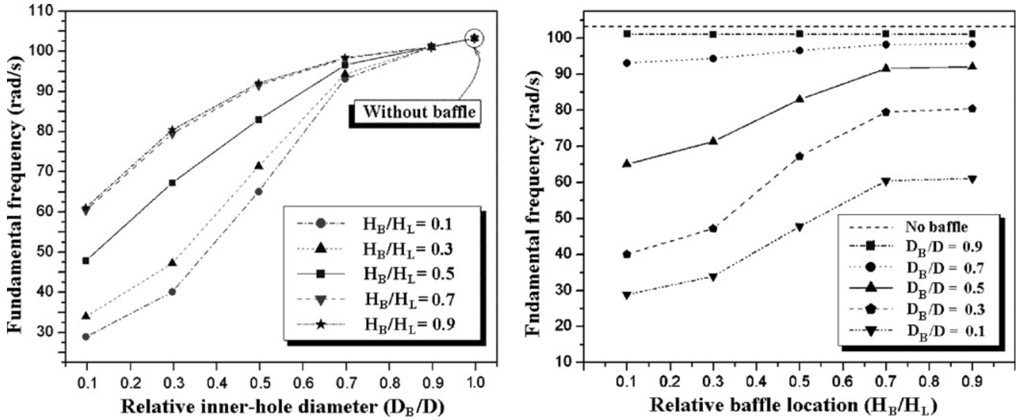

Figure 15. Variations of the fundamental frequency for one-baffle case: (a) to the relative inner-hole diameter D_B/D; (b) to the relative baffle location H_B/H_L.

the relative liquid fill height H_L/H of 0·9, and five relative baffle locations $H_B/H_L = 0{\cdot}1$, 0·3, 0·5, 0·7 and 0·9, and five relative baffle inner-hole diameters $D_B/D = 0{\cdot}1$, 0·3, 0·5, 0·7 and 0·9. Finite element meshes and boundary condition as well as geometry and material data are taken same as the previous one baffle case.

Figure 15(a) presents the variation of fundamental frequency with respect to the relative inner-hole diameter, where the fundamental frequency decreases uniformly as the baffle inner hole becomes smaller, and furthermore which becomes considerable as the baffle location becomes lower. This is because the added mass transformed from the hydrodynamic pressure becomes larger according to the increase of baffle surface interfacing with liquid, and next the hydrodynamic pressure in the fundamental mode, as shown in Figure 12(b), increases in reverse proportional to the vertical location.

Figure 15(b) shows the variation of fundamental frequency to the relative baffle location H_B/H_L. The fundamental frequency increases remarkably up to $H_B/H_L = 0{\cdot}7$, but after that its variation does not look noticeable. Of course, the variation becomes larger with the inner-hole diameter decrease. For a given baffle inner-hole size (i.e., for the same baffle surface area interfacing with liquid), the total hydrodynamic pressure acting on baffle becomes smaller as the baffle location becomes higher. As a result, the total equivalent mass of liquid added to the structure becomes smaller, and which increases the fundamental frequency.

Meanwhile, we want to emphasize that the variation of fundamental frequency is considerable either the relative inner-hole diameter $D_B/D < 0{\cdot}7$ or the baffle is located at $0{\cdot}3 \leqslant H_B/H_L \leqslant 0{\cdot}7$.

6. CONCLUSIONS

According to the symmetric structural-acoustic finite element formulation, free-vibration characteristics of liquid-storage tanks with and without baffle have been investigated. In order for the locking-free robustness as well as the numerical simplicity of the test FEM program, which is based upon degenerated shell elements and 3-D quadratic acoustic elements, the reduced integration (RI) technique and the modified shear correction factor (MSCF) were combined in the coupled symmetric two-field formulation.

Reliability of the test program and our theoretical work has been verified through the comparison with analytical solution of axisymmetric cylindrical tank, from which the maximum relative error in 10 lowest natural frequencies has been found to be $<3\%$ for various combinations of tank parameters. According to the locking test, the combination of the reduced integration and the shear correction factor for degenerated shell elements produced almost locking-free natural frequencies up to the ultra-thin relative thickness. As well as, we confirmed that the membrane-dominated vibration problem does not produce the numerical locking in natural frequencies.

Natural frequencies and modes of cylindrical tanks were parametrically examined, with respect to the baffle number and location, the baffle inner-hole diameter, as well as the liquid fill height. According to the parametric numerical results the following main observations are drawn:

1. From the parametric experiment of no-baffled tank, we found that the structural-acoustic free vibration is fundamentally composed of four distinguished modes: the low-plate-dominated, the upper-plate-dominated, the side-shell-dominated and mixed modes. Furthermore, the UPD mode generates a zero hydrodynamic-pressure mode, and it is influenced only by the baffle inner-hole size. Meanwhile, the SSD mode and the MIX mode are significantly affected by the liquid fill height.
2. The natural frequency of baffled tanks decreases with the baffle number, particularly in lower frequency range, so that the appearance of the first UPD mode, with the same natural frequency regardless of the baffle number, delays by one with the baffle number increase. However, all baffled tanks start with the fundamental mode that is dominated by the bottom plate and the lowest baffle, hence the lowest one among baffles experiences the largest hydrodynamic pressure interaction.
3. The fundamental frequency of one-baffled tank decreases uniformly as the baffle inner-hole diameter decreases, particularly when $D_B/D \leqslant 0{\cdot}7$, and furthermore this trend becomes crucial as the baffle location becomes lower. The reason has been found that

the equivalent mass of liquid added to the structure becomes larger as either the baffle inner-hole size decreases or the baffle location becomes lower. On the other hand, the fundamental frequency of one-baffled tank increases in proportional to the baffle height, particularly when $0{\cdot}3 \leqslant H_B/H_L \leqslant 0{\cdot}7$, and this variation becomes more significant as the baffle inner-hole size decreases.

ACKNOWLEDGMENTS

The financial support for this work by Agency for Defense Development under Contract No. ADD-00-5-6 is gratefully acknowledged.

REFERENCES

1. R. W. Lewis, P. Bettess and E. Hinton 1984 *Numerical Methods in Coupled Systems*. Chichester, U.K.: Wiley.
2. M. Amabili, M. P. Paidoussis and A. A. Lakis 1998 *Journal of Sound and Vibration* **213**, 259–299. Vibrations of partially filled cylindrical tanks with ring-stiffeners and flexible bottom.
3. J. Mackerle 1999 *Finite Elements in Analysis and Design* **31**, 231–240. Fluid–structure interaction problems, finite element and boundary element approaches—a bibliography (1995–1998).
4. H. J.-P. Morand and R. Ohayon 1995 *Fluid–Structure Interaction—Applied Numerical Methods*. New York: John Wiley & Sons.
5. Y. Calayir, A. A. Dumanoglu and A. Bayraktar 1996 *Computers & Structures* **59**, 877–890. Earthquake analysis of gravity dam–reservior systems using the Eulerian and Lagrangian approaches.
6. J. R. Cho and J. M. Song 2001 *Journal of Sound and Vibration* **239**, 995–1012. Assessment of classical numerical models for the separate fluid–structure modal analysis.
7. M. A. Haroun and M. A. Tayel 1985 *Earthquake Engineering and Structural Dynamics* **13**, 583–595. Response of tanks to vertical seismic excitations.
8. F. Welt and V. J. Modi 1992 *Journal of Vibration and Acoustics* **114**, 10–16. Vibration damping through liquid sloshing. part I: a non-linear analysis.
9. A M. Silveira, D. G. Stephens and H. W. Leonard 1961 *NASA Technical Note D*-715. An experimental investigation of liquid oscillation in tanks with various baffles.
10. O. C. Zienkiewicz and P. Bettess 1978 *International Journal for Numerical Methods in Engineering* **13**, 1–16. Fluid–structure dynamic interaction and wave forces.
11. G. C. Everstine 1997 *Computers & Structures* **65**, 307–321. Finite element formulations of structural acoustics problems.
12. H. J.-P. Morand and R. Ohayon 1979 *International Journal for Numerical Methods in Enginering* **14**, 741–755. Substructure variational analysis of the vibrations of coupled fluid–structure systems. Finite element results.
13. G. Sandberg and P. Goransson 1988 *Journal of Sound and Vibration* **123**, 507–515. A symmetric finite element formulation for acoustic fluid–structure interaction analysis.
14. L. G. Olson and K. J. Bathe 1985 *Computers & Structures* **21**, 21–32. Analysis of fluid–structure interactions. A direct symmetric coupled formulation based on the fluid velocity potential.
15. H. C. Chen and R. L. Taylor 1990 *International Journal for Numerical Methods in Engineering* **29**, 683–698. Vibrational analysis of fluid–soil systems using a finite element displacement formulation.
16. A. Gedikli and M. E. Erguven 1999 *Journal of Sound and Vibration* **223**, 141–155. Seismic analysis of a liquid storage tank with a baffle.
17. F. Welt and V. J. Modi 1992 *Journal of Vibration and Acoustics* **114**, 17–23. Vibration damping through liquid sloshing. part II: experimental results.
18. R. J. Hung and H. L. Pan 1995 *Journal of Spacecraft and Rockets* **32**, 723–731. Baffle effect on sloshing-modulated torques responsed to orbital accelerations in microgravity.
19. D. V. Evans and P. McIver 1987 *Journal of Fluid Mechanics* **175**, 295–307. Resonant frequencies in a container with a vertical baffle.

20. J. R. Cho, J. M. Song and J. K. Lee 2001 *Finite Elements in Analysis and Design* **37**, 467–483. Finite element techniques for the free-vibration and seismic analysis of liquid-storage tanks.
21. J. R. Cho, K. W. Kim, J. K. Lee, T. H. Park and Y. W. Lee *International Journal for Numerical Methods in Engineering*. Axisymmetric modal analysis of liquid-storage tanks considering flow compressibility (to appear).
22. M. S. Howe 1998 *Acoustics of Fluid–Structure Interaction*. New York: Cambridge University Press.
23. G. W. Housner 1963 *Bulletin of Seismic Society of America* **53**, 381–387. The dynamic behavior of water tanks.
24. J. R. Cho and J. T. Oden 1996 *Mathematical and Computer Modelling* **23**, 117–136. A priori modeling error estimates of hierarchical models for elasticity problems for plate- and shell-like structures.
25. S. Ahmad, B. M. Irons and O. C. Zienkiewicz 1970 *International Journal for Numerical Methods in Engineering* **2**, 419–451. Analysis of thick and thin shell structures by curved finite elements.
26. R. H. MacNeal 1998 *Finite Elements in Analysis and Design* **30**, 175–186. Perspective on finite elements for shell analysis.
27. J. N. Reddy and A. Miravete 1995 *Practical Analysis of Composite Laminates*. Tokyo: CRC Press.
28. B. A Szabo and I. Babuska 1994 *Finite Element Analysis*. New York: John Wiley & Sons.
29. J. R. Cho and J. T. Oden 1997 *Computer Methods in Applied Mechanics and Engineering* **149**, 33–48. Locking and boundary layer in hierarchical models for thin elastic structures.
30. O. C. Zienkiewicz, J. Too and R. L. Taylor 1971 *International Journal for Numerical Methods in Engineering* **3**, 275–290. Reduced integration technique in general analysis of plates and shells.